AGU100 ADVANCING EARTH AND SPACE SCIENCE

Geophysical Research Letters

RESEARCH LETTER
10.1029/2018GL081061

The Formation of a Dry-Belt in the North Side of Central Himalaya Mountains

Yan Wang[1], Kun Yang[1,2], Xu Zhou[2], Binbin Wang[2], Deliang Chen[3], Hui Lu[1], Changgui Lin[3], and Fuqing Zhang[4]

[1]Ministry of Education Key Laboratory for Earth System Modeling, Department of Earth System Science, Tsinghua University, Beijing, China, [2]CETES, Institute of Tibetan Plateau Research, Chinese Academy of Science, Beijing, China, [3]Regional Climate Group, Department of Earth Science, University of Gothenburg, Gothenburg, Sweden, [4]Department of Meteorology and Atmospheric Science, Pennsylvania State University, University Park, PA, USA

Key Points:
- A distinct dry-belt was found in the north of the central Himalaya Mountains
- The dry-belt is mainly due to the depletion of water vapor over the south slope of the Himalaya Mountains
- The foehn wind can postpone the diurnal cycle of the precipitation in the north side of the Himalaya Mountains

Supporting Information:
- Supporting Information S1

Correspondence to:
K. Yang,
yangk@tsinghua.edu.cn

Citation:
Wang, Y., Yang, K., Zhou, X., Wang, B., Chen, D., Lu, H., et al. (2019). The formation of a dry-belt in the north side of central Himalaya Mountains. *Geophysical Research Letters*, *46*, 2993–3000. https://doi.org/10.1029/2018GL081061

Received 24 OCT 2018
Accepted 27 FEB 2019
Accepted article online 4 MAR 2019
Published online 13 MAR 2019

Abstract South Asian monsoon crosses the Himalayan Mountains (HMs) and brings moisture for precipitations in the South Tibetan Plateau. A distinct dry-belt was found in the north of the central HM region, where there are the highest and steepest mountains in the world. Through in situ and remote-sensing observations and convection-permitting numerical experiments, the current study demonstrates that the formation of the dry-belt is mainly due to the depletion of water vapor when the monsoonal flow climbs the steep south slope of the HMs. The foehn phenomenon is notable over the north slope of the HMs, but the hot and dry downslope flow does not significantly reduce the amount of the precipitation; instead, it can delay the peak of the diurnal precipitation in the north side of the HMs.

Plain Language Summary The central Himalaya Mountains (HMs) possess the highest and steepest mountains. Recent in situ and remote-sensing observations show a dry-belt in the north side of the central HMs. Although it is plausible to speculate that the dry-belt results from the foehn wind on the leeside of the HMs, this study shows that the formation of the dry-belt is mainly caused by the drastic depletion of water vapor along the south slope of central HMs. The foehn wind mainly delays the diurnal peak of precipitation but hardly reduces the amount of precipitation.

1. Introduction

Precipitation in mountains directly affects hydrological processes and water resources downstream (Curio & Scherer, 2016). The central Himalayas possess the world highest and steepest mountains (e.g., Mt. Everest), where local precipitation and its variability may be influenced by many factors, such as the monsoon variability, mountain-valley winds, and local evaporation (Dai et al., 2002; Dai & Deser, 1999). Previous studies (Bookhagen & Burbank, 2006; Shrestha et al., 2012; Yang et al., 2018) show that mesoscale-to-microscale terrain variability in the Himalayan Mountains (HMs) can result in intensive spatial variability of precipitation.

In addition, the HMs may exert two effects on the spatial variability of precipitation in this region. First, the high HMs act as a barrier of the water vapor transport into the Tibetan Plateau (TP) during the monsoon season, resulting in much less precipitation in the TP than in its south region (Lin et al., 2018). Moreover, the microscale complex terrain variability in the south can induce strong turbulent orographic form drag, which weakens wind speed and associated water vapor transport over the HMs and thus reduces the precipitation over the TP (Zhou et al., 2017; Zhou et al., 2018). Second, *foehn* wind might be another factor that affects precipitation in the leeside. A foehn wind is characterized by the dry and hot downslope flow over the leeside of mountains that is caused by a dry adiabatic temperature lapse rate (Brinkmann, 1971). The foehn wind can influence variabilities of local and surrounding temperature and winds at temporal scales from hourly to seasonally (Cape et al., 2015; Speirs et al., 2013), which can influence agriculture, ecosystem natural disaster, and so forth (Langford et al., 2015). Nevertheless, theories about foehn wind are mostly based on sporadic cases and those studies mainly focus on air temperature and humidity (Armenta Porras, 2013; Cape et al., 2015; Gaffin, 2007; King et al., 2017; Turton et al., 2018). As far as we know, few studies have been performed on the features of foehn wind and its impact on precipitation over the HMs.

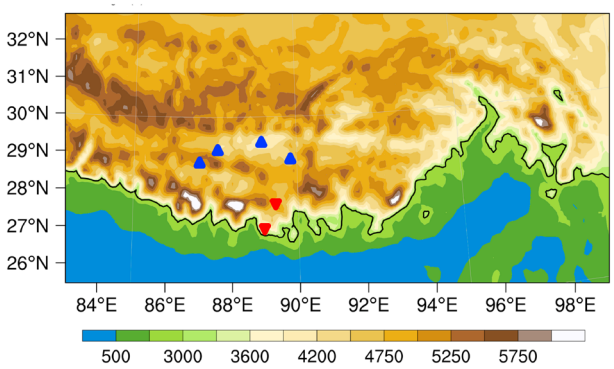

Figure 1. The terrain height (m) of south Tibetan Plateau in simulation of Weather and Research Forecasting (WRF) control case. The black line denotes the contour of 3,000 m asl, the blue triangles denote the locations of China Meteorological Administration stations (Dingri site: 87.08°E, 28.83°N, 4,300 m asl; Jiangzi site: 89.60°E, 28.92°N, 4,040 m asl; Lazi site 87.60°E, 29.08°N, 4,000 m asl; Rikaze site: 88.88°E, 29.25°N, 3,826 m asl), and the red triangles denote the locations of Global Positioning System stations (XYDX site: 88.94°E, 27.42°N, 2,993 m asl; DNLG site: 89.26°E, 27.90°N, 4,494 m asl).

In this study, a dry-belt in the northside of central HMs was first identified based on a satellite product of precipitation. Then, a numerical model (Weather and Research Forecasting [WRF] version 3.7) and in situ observations were used to explore the cause of the formation of the dry-belt. We conclude that it is the water vapor depletion over the south slope of the central HMs that causes the dry-belt in the northside, and the primary effect of foehn wind is reflected only in the diurnal variation of precipitation but not in the total amount of precipitation.

2. Data and Method

2.1. Data

The terrain of the region of interest is shown in Figure 1. It shows very complex terrain, with many mountains and valleys along the HM Ranges. The south slope of the HMs is very steep, and the elevation ranges over several hundred meters to more than 8 km above sea level (asl). The north slope is less steep, with an elevation drop about 4 km.

Three types of observational data were used in the analysis: (1) the National Aeronautics and Space Administration Global Precipitation Measurement (GPM) mission product (Hou et al., 2014; Huffman et al., 2014; Huffman et al., 2015), with a temporal resolution of 30 min and a spatial resolution of 0.1°. In this study, the GPM data during the summers of 2014–2017 were used to analyze the spatial pattern of precipitation over the south TP. (2) Precipitable water vapor (PWV) observed at two GPS stations. One is located at the HMs south slope (named as XYDX: 88.94°E, 27.42°N, 2,993 m asl) and the other at the north (named as DNLG: 89.26°E, 27.90°N, 4,494 m asl). We set up the two stations to observe the difference of PWV before and after the monsoonal water vapor crosses the central HMs and to evaluate WRF performance. (3) Precipitation data at four China Meteorological Administration (CMA) stations that are at the north slope of the HMs. The four stations are: Dingri site (87.08°E, 28.83°N, 4,300 m asl), Jiangzi site (89.60°E, 28.92°N, 4,040 m asl), Lazi site (87.60°E, 29.08°N, 4,000 m asl), Rikaze site (88.88°E, 29.25°N, 3,826 m asl). The focused period covers the summer (1 June to 31 August, JJA) in 2015, with a sampling interval of 30 min, and the accumulated precipitation in three h is obtained. These high temporal resolution data were used to analyze the diurnal variations of precipitation. The locations of two GPS stations and four CMA stations are shown in Figure 1.

2.2. Method

We use the advanced research version of WRF model to investigate water vapor depletion in the south and the foehn wind in the north side of the HMs. According to Maussion et al. (2014), high-resolution WRF simulations can better capture the precipitation pattern over the HMs and the surrounding areas than the satellite retrieved precipitation products such as from the Tropical Rainfall Measurement Mission (TRMM), especially for light intensity of precipitation. High-resolution WRF simulations have advantages in depicting the effects of steep terrain on precipitation and water vapor transport toward the TP (Collier & Immerzeel, 2015; Gao et al., 2015; Ma et al., 2015; Maussion et al., 2011). And, Armenta Porras (2013) used WRF to investigate foehn wind and its impact in the upper Magdalena. These studies demonstrate the usefulness of using WRF as a diagnostic tool used in the current study.

In this study, the ERA-interim (Dee et al., 2011) produced by the European Centre for Medium-Range Weather Forecasts (ECMWF) was used to drive the WRF model. Two one-way-nested domains of WRF simulations were designed, as indicated by D1 and D2 in Figure A1. The simulations for D1 and D2 use a spatial resolution of 30 km and 10 km, respectively. The model configurations for D1 and D2 simulations can be referred to Lin et al. (2018). The simulation period is from 00:00 26 May to 00:00 1 September 2015, and the first six days are treated as the spin-up time. The 10-km resolution WRF simulation for D2 (the same as in Figure 1) was analyzed.

In order to understand the dominant driving factor of the dry-belt in the north side of the HMs, we designed two WRF sensitivity experiments (named as the control case and filled case, respectively) in D2 to compare

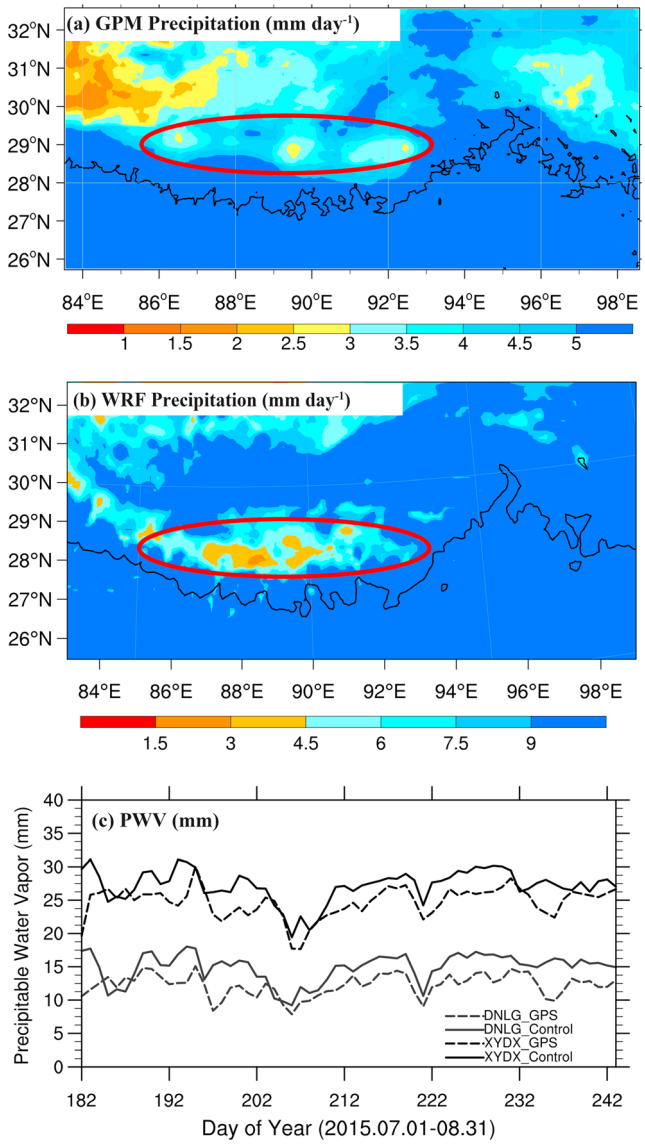

Figure 2. (a) Spatial pattern of Global Precipitation Measurement (GPM) daily precipitation (mm/day) averaged over the summers (June–August) of 2014–2017. (b) Spatial pattern of the simulated precipitation (mm/day) in the Weather and Research Forecasting (WRF) control case. In panels (a) and (b), the black lines denote the contour of 3,000 m asl, and the red ovals in panels (a) and (b) denote the target of dry-belt. (c) Comparison of precipitable water vapor (PWV; mm) between the control case simulation and Global Positioning System observations at XYDX station located at the Himalayan Mountain south slope and DNLG station located at the Himalayan Mountain north slope.

the precipitation and water vapor transport between them. In the control case, the default orography was used, which comprises the valley in the north side of the HMs; while in the filled case, the valley was filled so as to remove the foehn phenomena over north slope of the HMs. In the filled case, the terrain height (point P) between the two highest points (A and B) along the same longitude (Figure A2) was interpolated according to the following equation,

$$\mathrm{HP}_F = \left(\mathrm{HA}_c + \frac{HB_c - HA_c}{N} \times i\right) \times 0.8 + HP_c \times 0.2 \qquad (1\text{-}1)$$

where HP_F and HP_c are the terrain heights of the filled case and the control case, respectively; HA_c and HB_c are the terrain heights at point A and point B in the control case, respectively; N is the total grid number from point A to point B; and i is grid number from point A to point P, along the direction toward point B.

3. Results

3.1. Observed Dry-Belt in the North

In order to understand the water cycle in the HMs, field campaigns were organized in every year since 2012 by our research team and collaborators. Through the field work, we found that the north side of the HMs is hotter and dryer than its surrounding area. The dry-belt can be demonstrated by the GPM data. In the north side of the central HMs, precipitation in the dry-belt is much less than its south and north during the summer of 2015 as shown in Figure 2a. The dry condition causes much sparser vegetation coverage in this region (not shown).

The control case WRF simulation can reproduce the observed dry-belt (28.5°—29.5°N; 86°—93°E), as shown in Figures 2a and 2b. And the simulated spatial pattern is broadly consistent with the GPM retrieval. Besides, we compared the PWV between the simulation and GPS observations at the south and north slopes of the central HMs, respectively. As shown in Figure 2c, the simulated PWV is similar to the GPS observations at the two stations in terms of both the magnitude and variations. Thus, the WRF simulation could also describe the spatial and temporal patterns of PWV well. Therefore, it is reasonable to use the WRF model to investigate the formation of the dry-belt.

Before investigating the formation of the dry-belt, the WRF model performance is first assessed. The model configuration (including the simulating period, domain, and dynamical/physical schemes) in control case of the current study is exactly the same as in Lin et al. (2018). They had compared the simulated precipitation against the in situ observations and detected systematic wet biases over TP (section 3.1 in Lin et al., 2018). Meanwhile, the dry-belt in GPM is less clear than that in WRF. This could be attributed to its low detection skill at high altitude over TP and its surrounding (Wang & Lu, 2016; Xu et al., 2017). Thus, it tends to underestimate the amount of light rain events. Nevertheless, the precipitation in WRF control case and GPM differs in the amount but generally consistent in the spatial pattern with respect to the dry-belt detected region. Besides, other studies also support the finding that WRF is capable of depicting the spatial pattern of precipitation over the TP (Maussion et al., 2014; Curio & Scherer, 2016; Ma et al., 2015; Collier & Immerzeel, 2015; Bookhagen & Burbank, 2006, Bookhagen & Burbank, 2010).

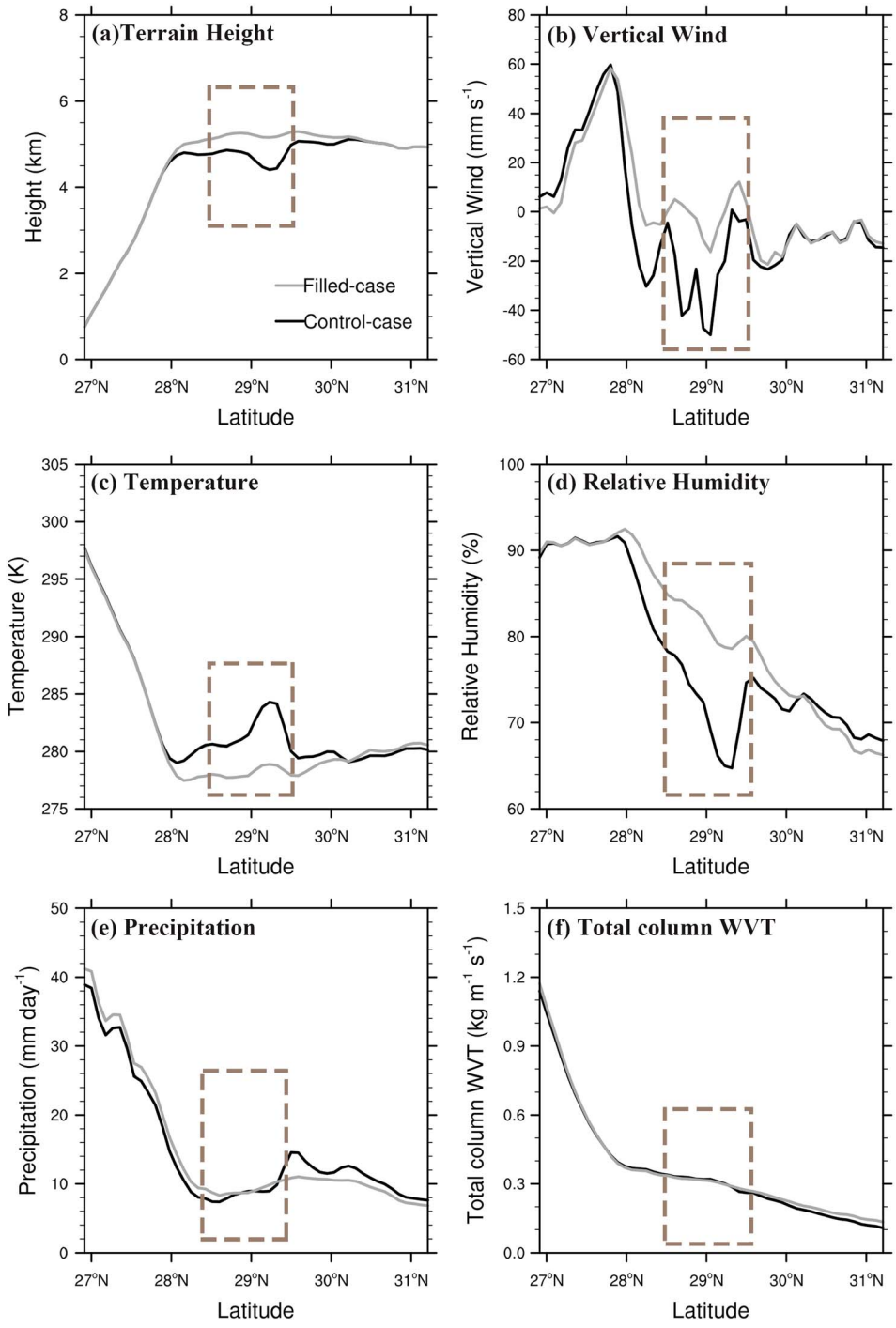

Figure 3. Comparisons between the control case simulation and the filled case simulation, averaged over 86–93°E during the simulation period (June-July-August 2015). (a) The terrain height (km), (b) vertical wind (mm/s), (c) air temperature (K) near the surface, (d) relative humidity (%) near the surface, (e) precipitation (mm/day), (f) total column water vapor transport (WVT; $kg \cdot m^{-1} \cdot s^{-1}$). The dashed rectangles in panels (a)–(f) denote the focus area of dry-belt.

3.2. Foehn Wind and Its Effects on Precipitation in the Dry-Belt

The dry-belt is located in a valley, with the central HMs to its south and Gangdise Mountains to its north, as indicated by the control case of Figure 3a. In the control case, the foehn features over the north slope are very distinct after the South Asian monsoon crosses the HMs: a prevailing downslope flow

(Figure 3b), higher temperature (Figure 3c), and lower relative humidity (RH; Figure 3d) than those over its adjacent regions. As the simulation in the control case, the temperature lapse rate over the south slope of central HMs is 4.8 ± 0.2 K/km, which is close to the typical value of the moist adiabatic lapse rate (Kittel & Kroemer, 1980); while that over the north slope is 9.6 ± 0.2 K/km, which is approximately equal to the constant dry adiabatic lapse rate (9.8 K/km; Minder et al., 2010). The average RH simulated in the control case in the dry-belt region (~65–75%) is lower than the one in the south slope of the HMs (>90%).

In the filled case (the valley is filled), however, the features of foehn wind over the dry-belt disappear: the downward speed over the dry-belt is close to zero (Figure 3b), the near-surface temperature is close to that in its adjacent region (Figure 3c), and the RH rises by about 5–15% relative to that in the control case (Figure 3d). Moreover, we compared the temperature and RH at the same altitude between the two cases and found that the temperature in the filled case is very close to that in the control case (not shown) and the RH in the filled case is still apparently higher than that in the control case (Figure A3). Therefore, it is confirmed that the foehn wind causes low RH values over the dry-belt region.

Nevertheless, there is no significant difference in the total amount of simulated precipitation in this dry-belt region between the two cases (Figure 3e), both of which are less than 10 mm/day. According to Figure 3d, the simulated RH in both cases is lower than 85% after crossing the central HMs. Therefore, it would be hard for water vapor to condense without appropriate air uplift, even in the filled case.

In short, foehn wind in the north side of the central HMs is clearly produced by the control case simulation, but the amount of precipitation in this region is not particularly sensitive to the existence of the foehn wind.

3.3. Water Vapor Attenuation When Crossing the Mountains

Water vapor condensation is a prerequisite of the generation of precipitation. There has been many studies in the water vapor transport (WVT) and precipitation over the TP. For example, Curio and Scherer (2016) indicated that the WVT from outside the region can contribute to about 40% precipitation over the TP. Bookhagen and Burbank (2006, 2010) showed that the high terrain is a barrier that rarely permits the water vapor to enter the TP and only the valleys over HMs are the primary vapor channels. The process of WVT is vital to the precipitation over the HMs (Curio & Scherer, 2016; Lin et al., 2018; Yang et al., 2018). Because of the high and steep topography along the south slope of the HMs, the water vapor depletes severely when crossing over the HMs (Lin et al., 2018; Yang et al., 2018). However, all of them did not elucidate the effect of vapor depletion on the formation of the foehn wind and the precipitation in the northside of the HMs. As shown in Figure 3d, the simulated RH in the control case over the south slope is more than 90% and often approaches 100% during JJA (not shown), which is consistent with observed one in Yang et al. (2018). When monsoonal warm and moist flow is forced to move upward along the south slope of the HMs, intensive precipitation occurs. As shown in Figure 3e, precipitations simulated in both cases are more than 20 mm/day in the whole south slope and can even reach more than 40 mm/day; in other words, a large amount of water vapor depletes over the south slope of the HMs.

In response to the water vapor condensation, the PWV decreases drastically along the south slope. As shown in Figure 2c, the mean value of PWV at DNLG site (4,494 m asl) is about 11.3 mm, less than half of that (24.8 mm) at XYDX site (2,993 m asl). Moreover, column-integrated WVT drops rapidly over the south slope of the HMs (Figure 3f). The WVT value averaged from 86 to 93°E through the cross section at 27.0°N with a mean elevation of about 1,000 m asl is 1.14 kg · m^{-1} · s^{-1}. When the water vapor reaches the ridge of the HMs (through the section of 28.07°N with a mean elevation of about 5,000 m asl), the total column of WVT is only 0.34 kg · m^{-1} · s^{-1} left. Therefore, more than 70% of water vapor attenuates when it moves from the foothills to the ridge of the central HMs. When water vapor enters the dry-belt, the total column WVT further decreases to 0.30 kg · m^{-1} · s^{-1} in both cases, as shown in Figure 3f. As both PWV and WVT are at a low level, it is not surprising that the precipitation in the dry-belt region is low.

In summary, both the observations and simulations indicate that only a small portion of water vapor can cross the central HMs. It is difficult to turn this much-below-saturation-point water vapor into precipitation if no significant synoptic-scale disturbances pass the dry-belt region.

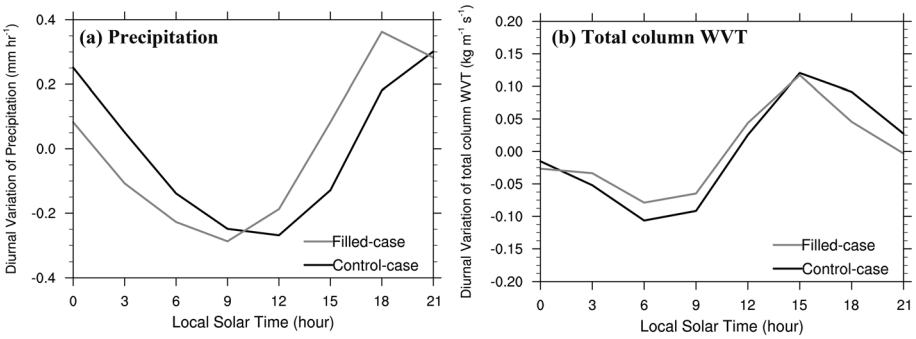

Figure 4. Comparison of the diurnal variations between the control case simulation and filled case simulation, averaged during the simulation period (June-July-August 2015). (a) Precipitation (mm/hr) after removing daily mean, averaged in dry-belt region; (b) total column WVT ($kg \cdot m^{-1} \cdot s^{-1}$) after removing daily mean, averaged over 86–93°E along the cross section at 27.9°N, where the water vapor through the section into the dry-belt region.

4. Discussion on the Role of Foehn Wind

Although the downslope flow over the north slope has limited impacts on the amount of precipitation in the dry-belt, it still plays a role in the diurnal cycle of precipitation.

According to the CMA station data and GPM products, the precipitation in the dry-belt region mainly occurs from late-afternoon to midnight (Figure A4). There is still system bias in depicting the diurnal water cycles of climate models (Yang & Slingo, 2001; Dai, 2006; Walther et al., 2013; Wang et al., 2017) and similarly 3 hr advance of precipitation in WRF simulation than CMA observation appears. But the pattern of diurnal variation (precipitation occurs from late afternoon to midnight) is well reproduced by the WRF simulation. Therefore, the difference between the two cases of WRF simulations can reflect the effect of the foehn wind on the diurnal variation of precipitation in the dry-belt.

As shown in Figure 4a, the amplitude of the precipitation diurnal cycle in the dry-belt is very similar in the two cases (~0.3 mm), but the peak of precipitation diurnal cycle in the control case (21:00 local time) is delayed about 3 hr, compared with the filled case (18:00 local time). Possible causes for the delay of precipitation peak are discussed below.

The precipitation diurnal cycle is controlled by multiscale orographic land-atmosphere interactions (Barros et al., 2004). Diurnal peaks of precipitation in mountainous regions are highly regulated by the thermally driven mountain-plain or mountain-valley circulations all over the world (e.g., He & Zhang, 2010; Bao et al., 2011). The first possible cause of the diurnal precipitation peak difference between the two simulations is the difference in the mountain-valley circulations. In the control case, solar heating on the north slope tends to drive the upslope flow, which may lift the water vapor and advance the precipitation peak instead of delaying it. So the mountain-valley circulations associated with the southern slope of the HMs is likely not a dominant factor for the difference in the precipitation peak shown in Figure 4a.

The second possible cause is the difference in the diurnal cycle of WVT between the two cases. We compared the total column WVT between the two cases at the cross-section of 27.9°N (Figure 4b), through which the vapor enters the dry-belt region. As shown in Figure 4b, the diurnal variation of WVT due to the terrain modification advances slightly but does not follow that of precipitation. Thus, the delay of precipitation peak in the control case is not due to the change in the WVT.

The third possible cause is that the foehn wind that exists in the control case but disappears in the filled case. We compared the precipitation diurnal cycle of the two WRF cases between the southside and northside of central HMs (Figure A5). Because the south side is very steep, we chose the region with the average height above 4,000 m to analyze the diurnal cycle. The precipitation over the southside occurs earlier than that over the north side. The simulated precipitation peak over high altitudes of the south side occurs in the afternoon (Figure A5a), which is consistent with the results of Barros et al. (2000) and Barros and Lang (2003). Besides, there is no distinct difference between the control case and filled case over the south side (Figure A5b). Over the southside, there is strong upslope flows during daytime associated with the strong thermal effect due to radiative heating. However, over the northside in dry-belt region, the strong attenuation of air water vapor

associated with the HMs leads to very limited water vapor during daytime. The foehn wind moves downslope, and it can suppress the lifting of water vapor and delay the occurrence of precipitation. Therefore, the foehn wind may be the cause of the delayed occurrence time of maximum precipitation in the north of the HMs.

5. Conclusions

In this study, a dry-belt in the northside of the central HMs is found with a satellite-retrieved precipitation product and is further reproduced by WRF simulations. The formation of the dry-belt is investigated with the WRF simulations. It is found that water vapor can be severely attenuated by the condensation process when crossing the central HMs into the TP. This process leads to the humidity being much below the saturation point and thus plays a more important role than the foehn wind in the formation of the dry-belt. Nevertheless, the foehn wind over the north slope can delay the occurrence of the diurnal precipitation in this region.

Acknowledgments
This work was supported by the Strategic Priority Research Program of the Chinese Academy of Sciences (grants XDA2006010201 and XDA20060401), National Natural Science Foundation of China (grants 91537210 and 41705084), Chinese Academy of Sciences (grant 131C11KYSB20160061), and the Swedish Foundation for International Cooperation in Research and Higher Education (grant CH2015-6226). The CMA data are obtained from the China National Meteorological Information Center (http://data.cma.cn/data/), and the GPM product is downloaded from the website of https://pmm.nasa.gov/GPM. The WRF model is documented at https://www.mmm.ucar.edu/weather-research-and-forecasting-model. The WRF output and the GPS retrieval in this paper are available under ftp://210.72.14.134/Public/ywang/wrf_out/.

References

Armenta Porras, G. E. (2013). Análisis detallado del efecto foehn generado por la cordillera Oriental en el alto Magdalena (Huila y Tolima). (Doctoral dissertation, Universidad Nacional de Colombia).

Bao, X., Zhang, F., & Sun, J. (2011). Diurnal variations of warm-season precipitation east of the Tibetan Plateau over China. *Monthly Weather Review*, *139*(9), 2790–2810. https://doi.org/10.1175/MWR-D-11-00006.1

Barros, A. P., Joshi, M., Putkonen, J., & Burbank, D. W. (2000). A study of the 1999 monsoon rainfall in a mountainous region in central Nepal using TRMM products and rain gauge observations. *Geophysical Research Letters*, *27*(22), 3683–3686. https://doi.org/10.1029/2000GL011827

Barros, A. P., Kim, G., Williams, E., & Nesbitt, S. W. (2004). Probing orographic controls in the Himalayas during the monsoon using satellite imagery. *Natural Hazards and Earth System Science*, *4*(1), 29–51. https://doi.org/10.5194/nhess-4-29-2004

Barros, A. P., & Lang, T. J. (2003). Monitoring the monsoon in the Himalayas: Observations in central Nepal, June 2001. *Monthly Weather Review*, *131*(7), 1408–1427. https://doi.org/10.1175/1520-0493(2003)131<1408:MTMITH>2.0.CO;2

Bookhagen, B., & Burbank, D. W. (2006). Topography, relief, and TRMM-derived rainfall variations along the Himalaya. *Geophysical Research Letters*, *33*, L08405. https://doi.org/10.1029/2006GL026037

Bookhagen, B., & Burbank, D. W. (2010). Toward a complete Himalayan hydrological budget: Spatiotemporal distribution of snowmelt and rainfall and their impact on river discharge. *Journal of Geophysical Research*, *115*, TC3002. https://doi.org/10.1029/2009JF001426

Brinkmann, W. A. R. (1971). What is a foehn? *Weather*, *26*(6), 230–240. https://doi.org/10.1002/j.1477-8696.1971.tb04200.x

Cape, M. R., Vernet, M., Skvarca, P., Marinsek, S., Scambos, T., & Domack, E. (2015). Foehn winds link climate-driven warming to ice shelf evolution in Antarctica. *Journal of Geophysical Research: Atmospheres*, *120*, 11,037–011,057. https://doi.org/10.1002/2015jd023465

Collier, E., & Immerzeel, W. W. (2015). High-resolution modeling of atmospheric dynamics in the Nepalese Himalaya. *Journal of Geophysical Research: Atmospheres*, *120*, 9882–9896. https://doi.org/10.1002/2015jd023266

Curio, J., & Scherer, D. (2016). Seasonality and spatial variability of dynamic precipitation controls on the Tibetan Plateau. *Earth System Dynamics*, *7*(3), 767–782. https://doi.org/10.5194/esd-7-767-2016

Dai, A. (2006). Precipitation characteristics in eighteen coupled climate models. *Journal of Climate*, *1*(18), 4605–4630. https://doi.org/10.1175/JCLI3884.1

Dai, A., & Deser, C. (1999). Diurnal and semidiurnal variations in global surface wind and divergence fields. *Journal of Geophysical Research*, *104*(D24), 31,109–31,125. https://doi.org/10.1029/1999JD900927

Dai, A., Wang, J., Ware, R. H., & Van Hove, T. (2002). Diurnal variation in water vapor over North America and its implications for sampling errors in radiosonde humidity. *Journal of Geophysical Research*, *107*(D10), 4090. https://doi.org/10.1029/2001JD000642

Dee, D. P., Uppala, S. M., Simmons, A. J., Berrisford, P., Poli, P., Kobayashi, S., et al. (2011). The ERA-Interim reanalysis: Configuration and performance of the data assimilation system. *Quarterly Journal of the Royal Meteorological Society*, *137*(656), 553–597. https://doi.org/10.1002/qj.828

Gaffin, D. M. (2007). Foehn winds that produced large temperature differences near the Southern Appalachian Mountains. *Weather and Forecasting*, *22*(1), 145–159. https://doi.org/10.1175/waf970.1

Gao, Y., Xu, J., & Chen, D. (2015). Evaluation of WRF mesoscale climate simulations over the Tibetan Plateau during 1979–2011. *Journal of Climate*, *28*(7), 2823–2841. https://doi.org/10.1175/jcli-d-14-00300.1

He, H., & Zhang, F. (2010). Diurnal variations of warm-season precipitation over northern China. *Monthly Weather Review*, *138*(4), 1017–1025. https://doi.org/10.1175/2010MWR3356.1

Hou, A., Kakar, R., Neeck, S., Azarbarzin, A., Kummerow, C., Kojima, M., et al. (2014). The global precipitation measurement mission. *Bulletin of the American Meteorological Society*, *95*(5), 701–722. https://doi.org/10.1175/BAMS-D-13-00164.1

Huffman, G. J., Bolvin, D. T., Braithwaite, D., Hsu, K., Joyce, R., & Xie, P. (2014). Algorithm Theoretical Basis Document (ATBD) Version 4.4 for the NASA Global Precipitation Measurement (GPM) Integrated Multi-satellitE Retrievals for GPM (I-MERG).

Huffman, G. J., Bolvin, D. T., & Nelkin, E. J. (2015). Integrated Multi-satellitE Retrievals for GPM (IMERG) Technical Documentation.

King, J. C., Kirchgaessner, A., Bevan, S., Elvidge, A. D., Kuipers Munneke, P., Luckman, A., et al. (2017). The impact of fohn winds on surface energy balance during the 2010–2011 melt season over Larsen C Ice Shelf Antarctica. *Journal of Geophysical Research: Atmospheres*, *122*, 12,062–12,076. https://doi.org/10.1002/2017JD026809

Kittel, C., & Kroemer, H. (1980). *Thermal physics* (2nd ed.). San Francisco: Freeman.

Langford, A. O., Pierce, R. B., & Schultz, P. J. (2015). Stratospheric intrusions, the Santa Ana winds, and wildland fires in Southern California. *Geophysical Research Letters*, *42*, 6091–6097. https://doi.org/10.1002/2015gl064964

Lin, C., Chen, D., Yang, K., & Ou, T. (2018). Impact of model resolution on simulating the water vapor transport through the central Himalayas: Implication for models' wet bias over the Tibetan Plateau. *Climate Dynamics*, *51*(9-10), 3195–3207. https://doi.org/10.1007/s00382-018-4074-x

Ma, J., Wang, H., & Fan, K. (2015). Dynamic downscaling of summer precipitation prediction over China in 1998 using WRF and CCSM4. *Advances in Atmospheric Sciences*, *32*(5), 577–584. https://doi.org/10.1007/s00376-014-4143-y

Maussion, F., Scherer, D., Finkelnburg, R., Richters, J., Yang, W., & Yao, T. (2011). WRF simulation of a precipitation event over the Tibetan Plateau, China-an assessment using remote sensing and ground observations. *Hydrology and Earth System Sciences*, *15*(6), 1795–1817. https://doi.org/10.5194/hess-15-1795-2011

Maussion, F., Scherer, D., Mölg, T., Collier, E., Curio, J., & Finkelnburg, R. (2014). Precipitation seasonality and variability over the Tibetan Plateau as resolved by the High Asia Reanalysis. *Journal of Climate*, *27*(5), 1910–1927. https://doi.org/10.1175/JCLI-D-13-00282.1

Minder, J. R., Mote, P. W., & Lundquist, J. D. (2010). Surface temperature lapse rates over complexterrain: Lessons from the Cascade Mountains. *Journal of Geophysical Research*, *115*, D14122. https://doi.org/10.1029/2009JD013493

Shrestha, D., Singh, P., & Nakamura, K. (2012). Spatiotemporal variation of rainfall over the central Himalayan region revealed by TRMM Precipitation Radar. *Journal of Geophysical Research*, *117*, D22106. https://doi.org/10.1029/2012JD018140

Speirs, J. C., McGowan, H. A., Steinhoff, D. F., & Bromwich, D. H. (2013). Regional climate variability driven by foehn winds in the McMurdo Dry Valleys, Antarctica. *International Journal of Climatology*, *33*(4), 945–958. https://doi.org/10.1002/joc.3481

Turton, J. V., Kirchgaessner, A., Ross, A. N., & King, J. C. (2018). The spatial distribution and temporal variability of föhn winds over the Larsen C Ice Shelf Antarctica Quarterly. *Journal of the Royal Meteorological Society*, *144*(713), 1169–1178. https://doi.org/10.1002/qj.3284

Walther, A., Jeong, J.-H., Nikulin, G., Jones, C., & Chen, D. (2013). Evaluation of the warm season diurnal cycle of precipitation over Sweden simulated by the Rossby Centre regional climate model RCA3. *Atmospheric Research*, *119*, 131–139. https://doi.org/10.1016/j.atmosres.2011.10.012

Wang, W., & Lu, H. (2016). Evaluation and comparison of newest GPM and TRMM products over Mekong River Basin at daily scale, 613–616. https://doi.org/10.1109/igarss.2016.7729153

Wang, Y., Yang, K., Pan, Z., Qin, J., Chen, D., Lin, C., et al. (2017). Evaluation of precipitable water vapor from four satellite products and four reanalysis datasets against GPS measurements on the southern Tibetan Plateau. *Journal of Climate*, *30*(15), 5699–5713. https://doi.org/10.1175/jcli-d-16-0630.1

Xu, R., Tian, F., Yang, L., Hu, H., Lu, H., & Hou, A. (2017). Ground validation of GPM IMERG and TRMM 3B42V7 rainfall products over southern Tibetan Plateau based on a high-density rain gauge network. *Journal of Geophysical Research: Atmospheres*, *122*, 910–924. https://doi.org/10.1002/2016jd025418

Yang, G.-Y., & Slingo, J. (2001). The diurnal cycle in the tropics. *Monthly Weather Review*, *129*(4), 784–801. https://doi.org/10.1175/1520-0493(2001)129,0784:TDCITT.2.0.CO;2

Yang, K., Guyennon, N., Ouyang, L., Tian, L., Tartari, G., & Salerno, F. (2018). Impact of summer monsoon on the elevation-dependence of meteorological variables in the south of central Himalaya. *International Journal of Climatology*, *38*(4), 1748–1759. https://doi.org/10.1002/joc.5293

Zhou, X., Beljaars, A., Wang, Y., Huang, B., Lin, C., Chen, Y., & Wu, H. (2017). Evaluation of WRF simulations with different selections of subgrid orographic drag over the Tibetan Plateau. *Journal of Geophysical Research: Atmospheres*, *122*, 9759–9772. https://doi.org/10.1002/2017jd027212

Zhou, X., Yang, K., & Wang, Y. (2018). Implementation of a turbulent orographic form drag scheme in WRF and its application to the Tibetan Plateau. *Climate Dynamics*, *50*(7–8), 2443–2455. https://doi.org/10.1007/s00382-017-3677-y